# Cylindrical High Pressure Xenon Spectrometer Using Scintillation Light Pulse Correction

Jeffrey L. Lacy, *Member, IEEE*, Athanasios Athanasiades, Nader N. Shehad, *Member, IEEE*,
Liang Sun, *Member, IEEE*, Tom D. Lyons, Christopher S. Martin, and Lu Bu

*Abstract*--**Cylindrical high-pressure xenon detectors utilizing Frisch grid electrodes have been employed for many years. These detectors are limited to no better than 2% energy resolution at 662 keV, a factor of 3 – 4 above the intrinsic spectroscopic limit of xenon. This likely results from imperfections in the structure of the Frisch grid combined with the high capacitive load which increases amplifier noise substantially.  Also, high sensitivity to microphonic noise of the sensitive grid severely limits field use. We propose a highly stable cylindrical structure consisting of concentric anode and cathode electrodes and use of scintillation light collected through a transparent end window. Measurement of the time interval between the prompt scintillation light from the interaction vertex and stimulated light produced by primary electrons arriving at the anode electrode provides determination of the radial deposited charge distribution, including effects of electron range and xenon fluorescence. In a 5 cm diameter detector employing a $MgF_2$ end window we have shown that anode signal levels can be corrected using the time digitized light output signal to achieve resolution superior to the Frisch grid systems and approaching the intrinsic xenon Fano limit. We anticipate employing the technique in arrays of kilogram scale detectors for high sensitivity high resolution field compatible gamma ray spectroscopy.**

*Index Terms* - **ionization detector, Frisch grid, gamma spectrometer, xenon**

## I. INTRODUCTION

IN a cylindrical ionization detector, measurement of the radial coordinate of Compton and photoelectric interactions can be used to correct field effects that otherwise degrade energy resolution. While $n_0$ electrons are freed in the medium by an ionizing interaction vertex, fewer than $n_0$ electrons are sensed by the anode amplifier.  The number delivered is only equal to $n_0$ if the electrons are deposited very near the cathode, and they drift through the entire potential difference between cathode and anode.  At any other radius, only a fraction is delivered, varying from one, for a radius equal to the cathode radius, diminishing to zero, as the radius approaches the anode radius. Figure 1 (left panel) shows this variation when an equal energy interaction occurs at different radial positions in a cylindrical detector with a cathode diameter of 4.8 cm and an anode diameter of 1.5 mm. The analytic form of this variation is given by expression 2 of section II. This variation severely degrades the energy resolution of the detector, as illustrated in the right panel of the figure, to approximately 10% FWHM for

a cathode to anode diameter ratio of 32. In contrast, the Fano limited energy resolution is 1.3% FWHM at 140 keV and 0.6% at 662 keV [1]. It should be noted from the pulse height distribution of Figure 1 that a large fraction of events deliver an appreciable fraction of their full deposited charge.
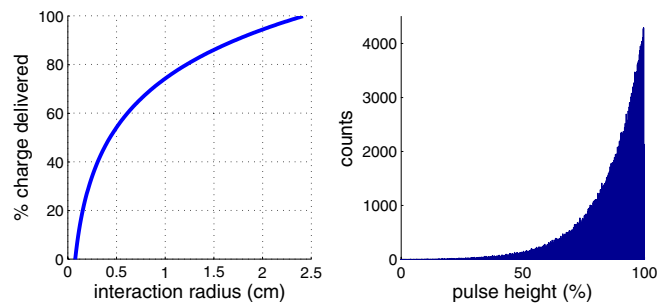


Figure 1. (left) The fraction of charge induced in the anode of a cylindrical ionization detector depends on the radius of interaction. (right) Pulse height spectrum of simulated gamma ray interactions, uniformly distributed within a cylindrical ionization detector. Even though all interactions deposited the same energy, the observed spread is large, due to the radial dependence plotted on the left.

Several groups [2]-[4] have employed a shielding (Frisch) grid that improves energy resolution in cylindrical ionization chambers, to levels of 2-4% at 662 keV. However, the intrinsic resolution offered by xenon has not been approached due to the high capacitance of the grid and its shielding inefficiencies. Such shielding grids are also notoriously sensitive to acoustic effects, preventing use in many field applications.

We propose a cylindrical ionization detector design that compensates for field effects by affording measurement of the drift time of the primary ionization electrons to the anode.  By measurement of the time lapse between the prompt 173 nm xenon scintillation light generated at the interaction vertex and the time of arrival of electrons at the anode, signaled by intense stimulated 173 nm scintillation in the high field in close proximity to the anode, radial position correction can be achieved. We further hypothesize that by measuring the detailed time history of the stimulated scintillation, the complex distribution of primary charge produced by Compton and photoelectron tracks and xenon fluorescence conversions can be accounted for (Figure 2).
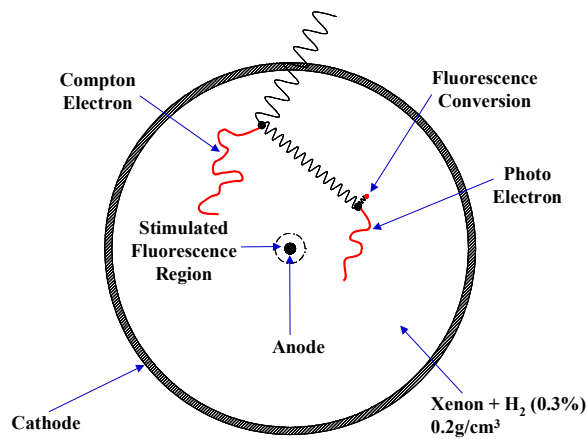
Figure 2. Typical multi-vertex event illustrating Compton vertex, photoelectric vertex, and fluorescence vertex, with the range of 6 mm for a 30 keV fluorescence photon.

## II. METHODS

### A. Detector design

A detector shown in Figure 3 was constructed and tested to evaluate the technique. It consists of a stainless steel (SS) tube, 50 mm in diameter, which contains xenon gas with 0.3% $H_2$ at a pressure of 30 atm (0.20 g/cm$^3$). One end of the cylinder incorporates a ceramic feedthrough that supports and seals around the SS anode. A metallic C-ring seal, installed between the ceramic and a SS compression flange, provides a high quality, epoxy-free seal that maintains xenon gas purity for long periods of time. The active length of the detector is 16 cm. Other components include copper guard rings that divert leakage currents away from the anode; gas and high-voltage ports; and a Teflon end cover for electrical insulation.
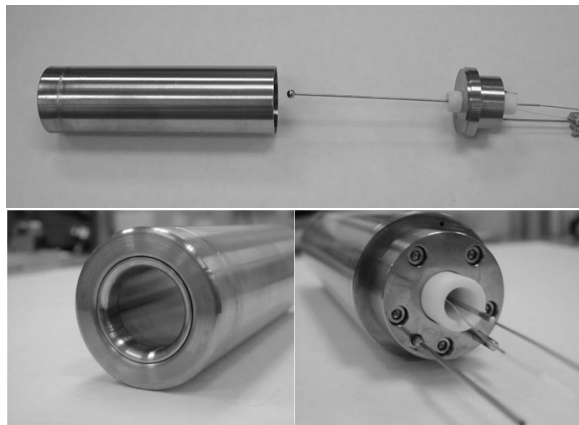


Figure 3. Photograph of prototype detector (top), showing the MgF$_2$ window (left) and the ceramic feedthrough for the anode (right).

The other end of the detector incorporates a MgF$_2$ crystal window, as shown in the schematic drawing of Figure 4. A light guide, machined out of Teflon (PTFE), fits over the end of the detector and mates directly with the photomultiplier tube

window. The system was operated in a high purity $N_2$ atmosphere to facilitate transmission of the 173 nm VUV scintillation light. The anode electrode, having a diameter of 1.5 mm, is terminated with a 6 mm diameter conductive sphere, whose diameter was chosen to maintain surface field continuity. Epoxy was used to achieve a seal between the crystal window and the stainless steel retainer wall. Small radioactive sources (1-3 µCi) were affixed to the wall of the detector during testing. The radioisotopes $^{22}$Na and $^{65}$Zn were attached in separate data collections providing a 511 keV annihilation line and an 1116 keV gamma line, respectively.

The detector cathode was biased to -19 kV, producing a field level of 2300 V/cm at the cathode. The stimulated scintillation threshold of $2.9 \times 10^{-17}$ V·cm$^2$ was reached at a radius of 2.1 mm, or 1.3 mm away from the anode surface (see Figure 2). At field levels $\geq$ 2300 V/cm in Xe, $H_2$ (0.3%), electron drift velocity is nearly completely saturated at a level of 3 µs/cm so that total drift time from cathode to anode is 7.5 µs [5].
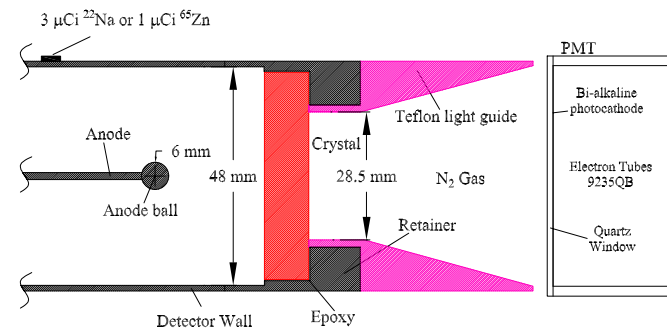


Figure 4. Schematic of prototype detector end showing the MgF$_2$ crystal window, Teflon light guide and photomultiplier tube window.

### B. Data acquisition

Signals induced in the anode were read with a specially designed charge sensitive amplifier carefully matched to the low 7 pF capacitance of the detector. This signal was shaped with a spectroscopy amplifier (Canberra 2022) using a 12 µsec shaping time constant. A noise level of ~100 electrons (rms) was achieved, contributing 1.0% FWHM at 511 keV and 0.46% FWHM at 1116 keV. Light signals were sensed with a photomultiplier tube (9235QB, Electron Tubes Ltd), as described above. Both charge and light signals were digitized with a 14-bit, $100 \times 10^6$ samples/s data acquisition board (National Instruments #5122), and subsequently processed in a computer. The digitizer was triggered from a timing single channel analyzer (Canberra 2037A) using as input, the bipolar output of the spectroscopy amplifier. Typical PMT signals are shown in Figure 5, where 100 signals are overlayed and both the primary and secondary (stimulated) emission pulses are indicated. The latter often contain multiple pulses with a complex time profile, due to the extended range and torturous path of Compton and photoelectrons in the gas, or due to multiple interaction vertices (Figure 2). The primary pulses, on

the other hand, have a narrow spread in time, as shown in Figure 6, and can thus serve as an accurate reference for time measurements. The decay time constant of the signal envelope shown in the figure is ~40 ns. Thus even in the event of detection of only one primary photon, start time is determined with high precision relative to electron drift velocity. On average, the prompt PMT signal had 21 detected photons at 511 keV and 45 detected photons at 1116 keV.
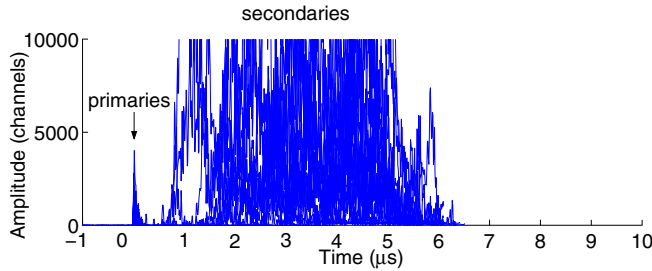


Figure 5. Multiple superimposed digitized traces of photomultiplier tube output showing prompt primary and delayed secondary scintillation light detected when 1116 keV gamma rays deposit their full energy in the detector.
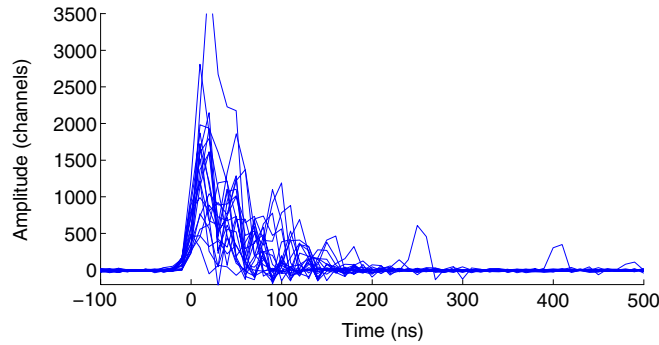


Figure 6. Blow up of the prompt portion of the PMT signal of Figure 5.

## C. *Pulse height correction algorithm*

The proposed method of pulse height correction is based on use of the analytical charge delivery versus collection radius together with known drift speed dependence on the electric field. The digitized PMT signal is employed to compute a correction factor which is applied to the precisely measured anode pulse height ($H$). The correction factor $C$ is

$$C = \frac{\sum_n A[n] \cdot \varphi(r[n])}{\sum_n A[n]} \qquad (1)$$

where $A[n]$ is the amplitude of the $n$th sample of the PMT digitized waveform, as shown in Figure 7, $r[n]$ is the radius associated with that sample, and $\varphi$ expresses the dependence of the pulse height on the radial position of the gamma interaction (plotted in Figure 1). For the cylindrical geometry this dependence can be written analytically as,

$$\varphi(r) = \frac{1}{\ln(b/a)} \cdot \ln(\frac{r}{a}) \qquad (2)$$

where $a$ and $b$ are the anode and cathode radii, respectively. The radius $r[n]$ corresponding to each time sample $t[n]$ is determined, accounting for the known dependence of the drift speed $\upsilon$ on the electric field, which has been reported in [5, 6] for a high pressure gas mixture of Xe/H$_2$ (0.25%). The formula used to solve for $r[n]$ is

$$t[n] = \int_a^{r[n]} \frac{1}{\upsilon(r)} dr \qquad (3)$$

Using Eq. 3, a table of correspondence between $t[n]$ and $r[n]$ was generated. The rapid correction algorithm employed is outlined as follows:

1. Digitize the anode charge pulse height $H$, and the corresponding PMT trace.
2. For each $t[n]$ in the PMT trace, look up the $r[n]$ corresponding to $A[n]$.
3. Compute $\varphi(r[n])$ using Eq. (2).
4. Compute the correction factor $C$, using Eq. (1).
5. Divide the pulse height $H$ by the correction factor $C$.

For analytical purposes it is also useful to compute a mean light signal time defined arbitrarily as the amplitude weighted mean of the light signal. A corresponding mean radius R is then derived by using Eq. 3. The value of R is not used in the correction algorithm, but is used in the correlation plots in the following section.
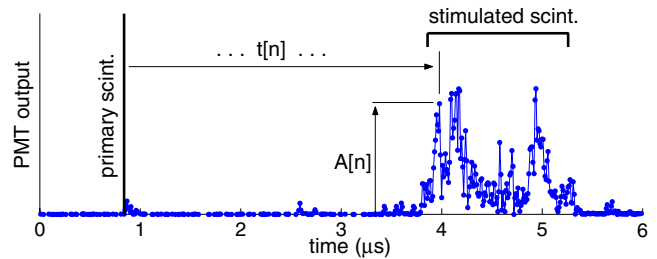


Figure 7. Typical digitized trace of photomultiplier tube output showing a probable multi-vertex event as illustrated in Figure 2. A vertical line marks the time of a small pulse due to primary scintillation in xenon. The delayed cluster of pulses generated by the stimulated emission is also marked. The pulse height correction algorithm uses the time $t[n]$ between the primary scintillation and each one of the samples in the cluster, together with the light amplitude of each cluster, $A[n]$.

## III.   RESULTS & DISCUSSION

The estimated mean radial coordinate R and corresponding anode pulse height ($H$) are plotted against one another in Figure 8. Both $^{22}$Na and $^{65}$Zn results obtained in separate acquisitions are shown together. A clear correlation is seen between energy and radius, in the form of narrow bands corresponding to the characteristic 511 keV and 1116 keV gammas emitted by each source. The correlation bands follow
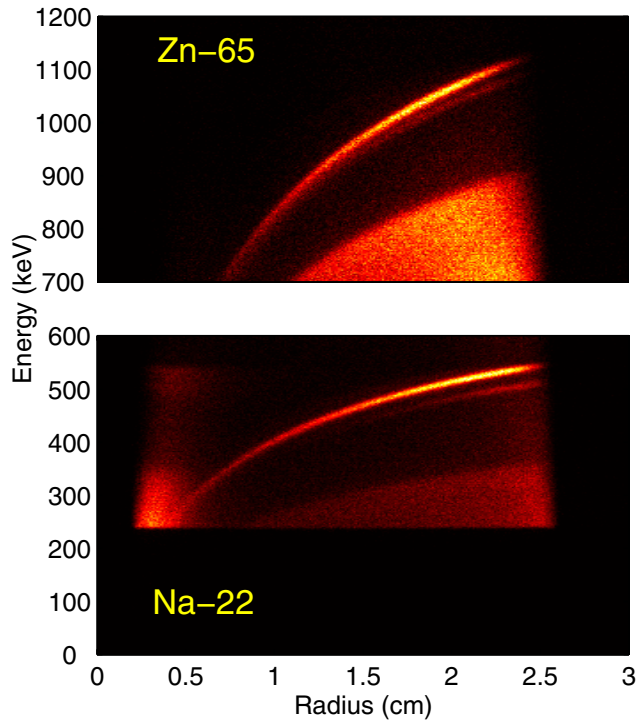
Figure 8. Mean radius (R) to pulse height correlation for $^{22}$Na and $^{65}$Zn gamma interactions in the prototype detector.
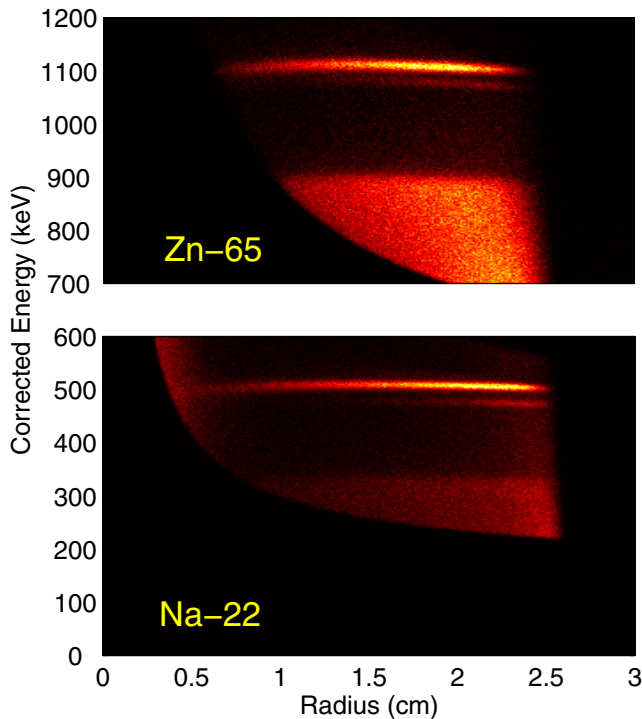


Figure 9. Mean radius (R) to pulse height correlation for $^{22}$Na and $^{65}$Zn gamma interactions in the prototype detector, following pulse height correction, as discussed in the text.

generally the analytical expression for φ (see Eq. 2). A very clear Compton edge associated with each band is also readily

observed. In addition xenon fluorescence escape bands are also apparent beneath the photo peak bands. These escape bands vanish at radii below about 2 cm, consistent with the 6 mm range of a 30 keV photon in 0.2 g/cm$^3$ xenon.
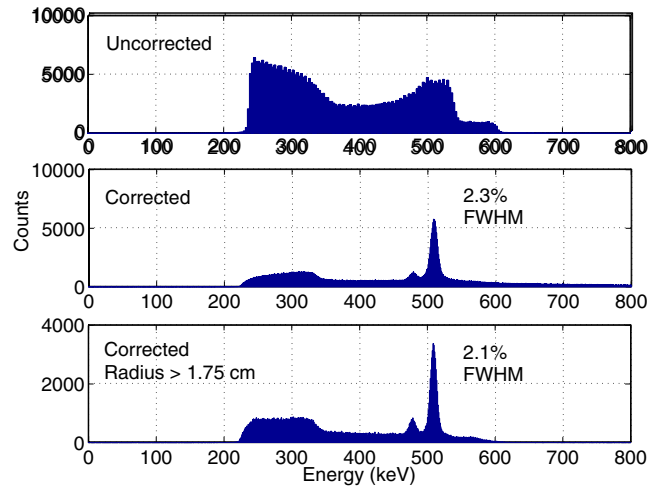


Figure 10. Uncorrected (top) and corrected (middle and bottom) energy spectra for a $^{22}$Na gamma source, collected in the prototype detector, at a bias of -19 kV. The middle panel shows the spectrum of all events of Figure 9 after empirical correction and the lower panel shows the subset of these events having radii (R) greater than 1.75 cm.
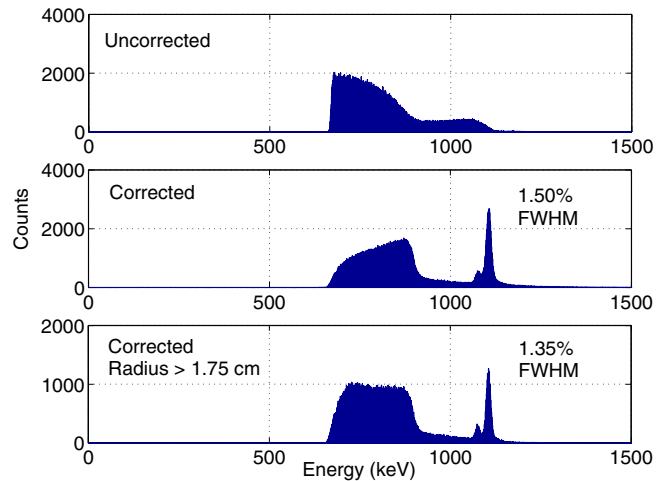


Figure 11. Uncorrected (top) and corrected (middle and bottom) energy spectra for a $^{65}$Zn gamma source, collected in the prototype detector, at bias of -19 kV. The middle panel shows the spectrum of all events of Figure 9 after empirical correction and the lower panel shows the subset of these events having radii (R) greater than 1.75 cm.

Using the algorithm described previously, the pulse height of each individual event was corrected producing the scatter plot in Figure 9. Note the very nearly flat correlation bands corresponding to 511 keV and 1116 keV. The projected energy spectra are shown for each source in Figure 10 and Figure 11. The top panels show the uncorrected spectra, exhibiting the expected poor energy resolution. The middle panels show the light corrected spectra after an additional empirical correlation correction was applied to remove the slight curvature in the

bands of Figure 9. The bottom panels show spectra for an approximately 50% subset of events having $R > 1.75$ cm. The corrected energy resolution at 511 keV is 2.3%. Further slight improvement in the resolution to a value of 2.1% is achieved in the radius limited data. The electronic noise during the measurements was approximately 100 electrons (RMS). This contributes about 1.0% to the spread of the peak (FWHM). The intrinsic resolution of xenon at this field level (2300 V/cm at the cathode) is 1.1% [1]. Combining these errors in quadrature predicts a resolution of 1.5%.
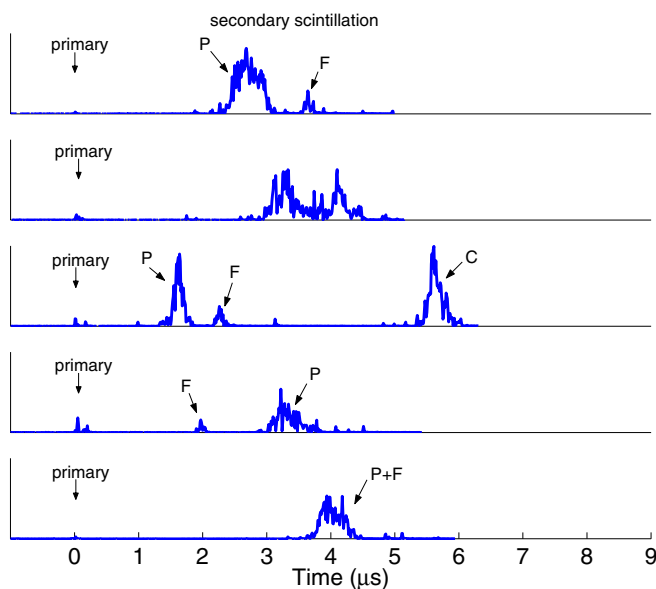


Figure 12. Typical PMT traces for 511 keV interactions with possible topologies indicated, P = photoelectric, C = Compton, F = fluorescence.
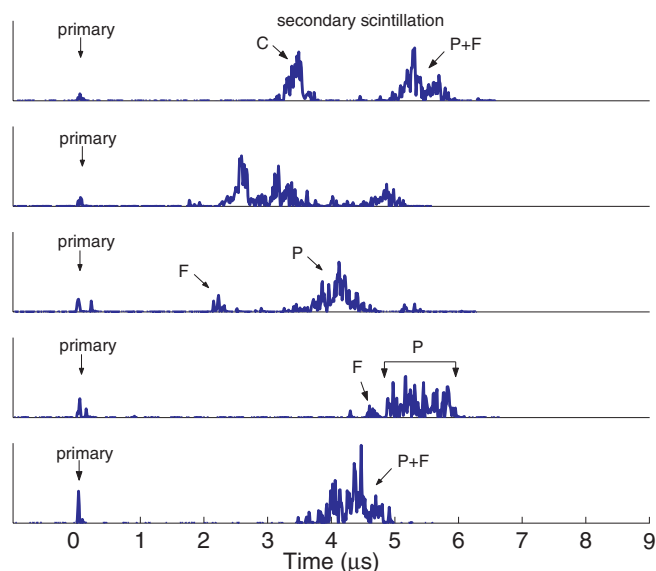


Figure 13. Typical PMT traces for 1116 keV interactions with possible topologies indicated, P = photoelectric, C = Compton, F = fluorescence.

For $^{65}$Zn (1116 keV), the corrected spectrum resolution is 1.5% for all events, and 1.35% for events limited to large radii.

The intrinsic resolution of xenon at this energy and field level is 0.8% [1]. When combined with a noise level of 0.46%, an experimental resolution of 0.92% is predicted.

Typical individual event PMT signals are shown in Figure 12 for 511keV and in Figure 13 for 1116 keV. Randomly selected events were taken from the clean photo peak regions shown in Figure 10 and Figure 11. Both the primary and secondary (stimulated) emission pulses are indicated. The latter often contain multiple and time extended pulses, as previously discussed. Photoelectric interactions are frequently accompanied by a fluorescence (30 keV) conversion, having a conversion range of 6 mm in 0.2 g/cm$^3$ xenon. Despite the complexity of these signals, the correction algorithm worked well, as it should, since each packet of collected charge is corrected individually.

## IV. CONCLUSION

In conclusion, we show that radial position encoding, based on timing of the primary and stimulated scintillations through utilization of a unique time weighted correction algorithm, can improve energy resolution significantly, in a cylindrical detector geometry, and that resolution levels at least as good and perhaps much better than Frisch grid systems can be achieved. The attractive Xe spectroscopic medium combined with the robust cylindrical structure, offers the prospect of field deployable kg scale high resolution detectors.

## V. REFERENCES

[1] A. Bolotnikov and B. Ramsey, "Development of high-pressure xenon detectors," in *Proceedings of SPIE*, San Diego, CA, 1998, vol. 3446, pp. 64-75.
[2] A. Bolotnikov and B. Ramsey, "Improving the energy resolution of high-pressure Xe cylindrical ionization chambers," *IEEE Trans. Nucl. Sci.*, vol. 44, pp. 1006-1010, 1997.
[3] K. F. Vlasik, I. V. Chernysheva, and V. V. Dmitrenko et. al., "Present status of cylindrical high pressure xenon gamma-ray spectrometers," in *Procs. International Seminar, High pressure xenon: fundamental research, detectors and their application*, Moscow, 2003, MEPHI, p. 221.
[4] G. Tepper, J. Losee, and R. Palmer, "A cylindrical xenon ionization chamber detector for high resolution, room temperature gamma radiation spectroscopy," *Nuclear Instruments and Methods in Physics Research*, vol. 413, pp. 467--470, 1998.
[5] V. V. Dmitrenko, A. S. Romanyuk, S. I. Suchkov, and Z. M. Uteshev, "Electron mobility in dense xenon gas," *Sov. Phys. Tech. Phys.* vol. 28, no. 12, pp. 1440--44, 1983.
[6] Z. M. Uteshev, V. V. Dmitrenko, A. S. Romanyuk, and S. I. Suchkov, "Measurements of electrons drift velocities in xenon-hydrogen mixtures," in *Procs. International Seminar, High pressure xenon: fundamental research, detectors and their application,* Moscow, 2003, MEPHI p. 194.